Supplementary Materials: Floquet-driven light transport in programmable photonic processors via discretized evolution of synthetic magnetic fields

Andrea Cataldo[1,*], Rohan Yadgirkar[1], Ze-Sheng Xu[1], Govind Krishna[1], Ivan Khaymovich[2], Val Zwiller[1], Jun Gao[1,*], and Ali W. Elshaari[1,*]

[1]Department of Applied Physics, KTH Royal Institute of Technology, Albanova University Centre, Roslagstullsbacken 21, Stockholm, 106 91, Stockholm, Sweden

[2]Nordita, KTH Royal Institute of Technology and Stockholm University, Hannes Alfvéns väg 11, Stockholm, 106 91, Stockholm, Sweden

[*]Corresponding author. Email: andreacl@kth.se, junga@kth.se, elshaari@kth.se

S1. Hamiltonian realization of the triangular plaquette

As discussed in the main text, the fundamental building block of our lattice is a three-site triangular plaquette. We define a set of hopping Hamiltonians $\{H_1, H_2, H_3\}$ that activate each edge sequentially:

$$H_1 = J(|1\rangle\langle 2| + |2\rangle\langle 1|), \quad H_2 = J(|2\rangle\langle 3| + |3\rangle\langle 2|), \quad H_3 = J(|3\rangle\langle 1| + |1\rangle\langle 3|), \tag{S1}$$

where J is the coupling strength and $|i\rangle$ represents a photon localized at site i. These Hamiltonians cycle with period T, each operating for duration $T/3$ before switching to the next, creating a time-periodic system $H(t) = H(t+T)$. Each subprocess evolves the system through the unitary operator:

$$U_k(T/3) = \exp(-iH_kT/3), \quad k = 1, 2, 3. \tag{S2}$$

The Floquet operator, $U_F(T)$, is the time-ordered product of these operators. Consequently, the clockwise (CW) modulation, corresponding to the sequence $H_1 \to H_2 \to H_3$, is distinct from its reversed, counter-clockwise (CCW) analog:

$$U_F^{\text{CW}}(T) = U_3U_2U_1, \qquad U_F^{\text{CCW}}(T) = U_1U_2U_3. \tag{S3}$$

For the stroboscopic evolution, the non-commuting drive sequence results in an effective Hamiltonian $H_{\text{eff}} = (i/T)\ln U_F(T)$ with complex hopping amplitudes:

$$H_{\text{eff}} = \sum_i V_{\text{eff}}^{(i)} |i\rangle\langle i| + \sum_{\langle i,j\rangle} \left(J_{\text{eff}}^{(ij)} e^{i\phi_{ij}} |i\rangle\langle j| + \text{h.c.} \right). \tag{S4}$$

Here, $V_{\text{eff}}^{(i)}$ are emergent on-site potentials and J_{eff} are effective coupling strengths. For larger lattices the effective Floquet Hamiltonian is not strictly short-range and, in principle, can include all-to-all terms; it is also not unique for a given $U_F(T)$. The phases ϕ_{ij} relate to the synthetic vector potential via $\phi_{ij} = \int_{\mathbf{r}_i}^{\mathbf{r}_j} \mathbf{A} \cdot d\mathbf{l}$.

Finally, static programmed phases, $\Phi_{\text{static}} = \sum_k \alpha_k$, are introduced by modifying the hopping terms of the constituent Hamiltonians:

$$H_k = J(e^{i\alpha_k}|i\rangle\langle j| + \text{h.c.}). \tag{S5}$$

so that both the dynamic and static contributions combine additively as the total Aharonov-Bohm phase accumulated in our lattice:

$$\Phi_{\text{total}} = \Phi_{\text{mod}} + \Phi_{\text{static}}. \tag{S6}$$

The principle established here can be readily applied to engineer programmable synthetic magnetic fields in larger systems composed of interconnected triangular plaquettes (following Fig. 1c in the main text).

S2. Device fabrication and specifications

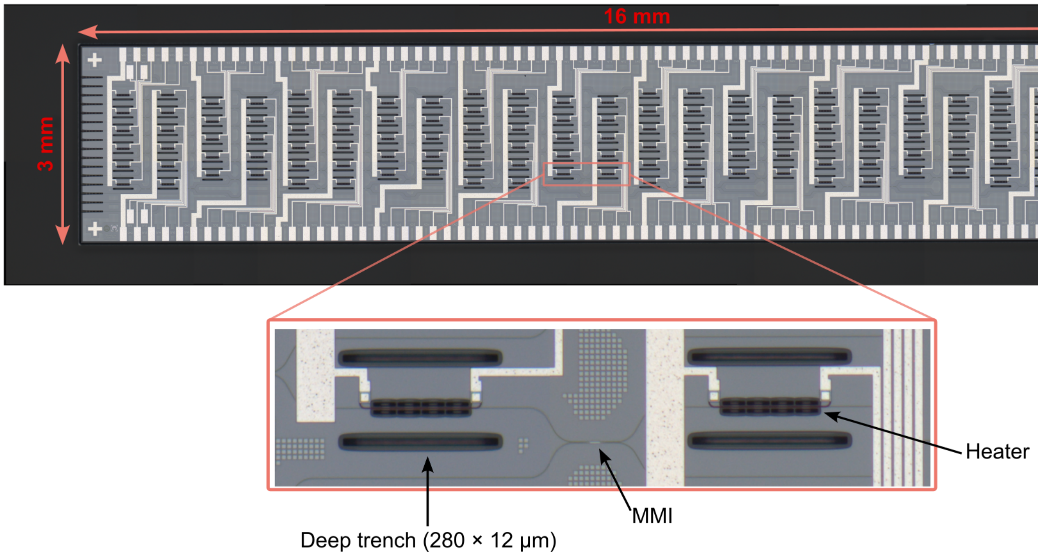

Fig. S1. Optical microscope image of the programmable photonic processor. The chip measures 16 $\times$ 3 mm and integrates 264 elements (phase shifters and MMIs). Deep trenches (280 $\times$ 12 µm) are etched around the MZIs to reduce thermal crosstalk between neighboring heaters. Inset: magnified view highlighting an MMI, a thermo-optic heater, and surrounding trenches.

The photonic chip (Fig. S1) was fabricated at Advanced Micro Foundry using their standard silicon-on-insulator platform with a 220 nm thick silicon layer above a 3 μm buried oxide substrate. It provided 12 input and 12 output waveguides (acting as the lattice sites) interconnected through a reconfigurable mesh of thermally-tuned MZIs controlled by precision multichannel current sources. The 500 nm wide waveguides supported single-mode operation in the C-band (1530-1565 nm) with typical propagation losses of 2 dB/cm. Edge couplers at the chip facets allowed fiber-to-chip coupling with losses of approximately 1.3 dB for TE polarization. The chip integrates 264 elements (phase shifters and multimode interferometers). Deep trenches (280 $\times$ 12 µm) were included around the MZIs to suppress thermal crosstalk between adjacent heaters.

S3. Experimental equipment specifications

The experimental control stack consisted of the following equipment:

- **Current Sources:** Qontrol Q8iv (8 channels per module, 740 nA precision).

- **Laser Source:** PicoQuant PDL 800-B (1550 nm, 50-70 ps FWHM pulse width, 40 MHz repetition rate, 3 mW average power).
- **Optical Switches:** FiberWDM 1×12 MEMS switches.
- **Detection:** Thorlabs PM100D meter with S122C germanium sensor (range 50 nW to 40 mW, responsivity $\sim$0.96 A/W).
- **Temperature Control:** Thorlabs TED200C PID controller using thermistor feedback targeting 10 kΩ with stability within ± 0.01°C.

S4. MZI transfer matrix derivation

The transfer matrix for the MZIs used in this work is derived here. The MZI consists of four components in series: an external phase shifter φ, a first 3-dB ideal coupler, an internal phase shifter θ, and a second 3-dB ideal coupler (Fig. S2).

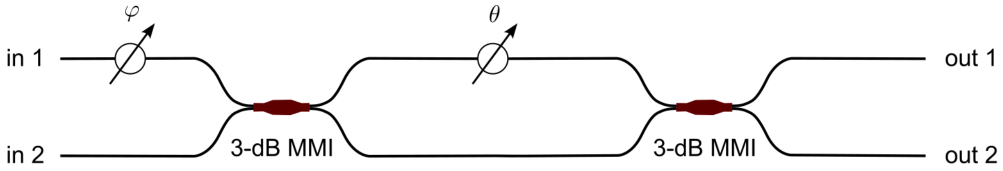

Fig. S2. Schematic of the MZI composed of two 3-dB MMIs and two thermo-optic phase shifters (φ, θ). Inputs and outputs labeled in 1–2, out 1–2.

The transfer matrices for the phase shifters and the ideal 3-dB coupler are defined as:

$$T_\varphi = \begin{bmatrix} e^{i\varphi} & 0 \\ 0 & 1 \end{bmatrix}, \quad T_\theta = \begin{bmatrix} e^{i\theta} & 0 \\ 0 & 1 \end{bmatrix}, \quad T_{\mathrm{C}} = \frac{1}{\sqrt{2}} \begin{bmatrix} 1 & i \\ i & 1 \end{bmatrix}. \tag{S7}$$

The total transfer matrix is the product of these individual components:

$$\begin{aligned} T_{\mathrm{MZI}} &= T_{\mathrm{C}} T_\theta T_{\mathrm{C}} T_\varphi \qquad \text{(S8)} \\ &= \left(\frac{1}{\sqrt{2}} \begin{bmatrix} 1 & i \\ i & 1 \end{bmatrix} \begin{bmatrix} e^{i\theta} & 0 \\ 0 & 1 \end{bmatrix} \right) \left(\frac{1}{\sqrt{2}} \begin{bmatrix} 1 & i \\ i & 1 \end{bmatrix} \begin{bmatrix} e^{i\varphi} & 0 \\ 0 & 1 \end{bmatrix} \right) \\ &= \frac{1}{2} \begin{bmatrix} e^{i\varphi}(e^{i\theta} - 1) & i(e^{i\theta} + 1) \\ ie^{i\varphi}(e^{i\theta} + 1) & 1 - e^{i\theta} \end{bmatrix}. \qquad \text{(S9)} \end{aligned}$$

Using the identities $e^{i\theta} - 1 = 2i\sin(\theta/2)e^{i\theta/2}$ and $e^{i\theta} + 1 = 2\cos(\theta/2)e^{i\theta/2}$, leads to the final result:

$$T_{\text{MZI}} = ie^{i\theta/2} \begin{bmatrix} e^{i\varphi}\sin(\theta/2) & \cos(\theta/2) \\ e^{i\varphi}\cos(\theta/2) & -\sin(\theta/2) \end{bmatrix}. \tag{S10}$$

S5. Unitary embedding and decomposition

Since our theoretical models utilize only a subset of the 12 available spatial modes, we embed the evolution operators into the full-dimensional space. For an n-site lattice with operator U_n acting on selected modes, the embedded 12×12 unitary takes the block-diagonal form:

$$U_{12} = \begin{bmatrix} U_n & 0 \\ 0 & I_{12-n} \end{bmatrix}, \tag{S11}$$

where I_{12-n} is the identity matrix for the unused waveguides. This ensures that light in inactive waveguides propagates unchanged while lattice dynamics occur exclusively in the active subspace. Physically, MZIs connecting to unused waveguides are set to maximum reflectivity $\theta = \pi$, preventing coupling between these waveguides.

The Clements decomposition [**?**] expresses this unitary as:

$$U_{12} = D \prod_{(m,n)\in S} T_{m,n}(\theta_{m,n}, \varphi_{m,n}), \tag{S12}$$

where D represents diagonal phase factors at the output ports, S denotes the ordered sequence of mode pairs, and each $T_{m,n}$ is the 12×12 matrix with the 2×2 block from Eq. (S10) acting on modes m and n. Applying this decomposition to our embedded evolution operators yielded the set of phase values $\{(\theta_{m,n}, \varphi_{m,n})\}$ that parameterize each MZI on the chip.

Realizing these target phase shifts from the unitary decomposition requires compensating for phase variations in each MZI through systematic calibration. The full characterization and fitting procedure for the current-phase relation is provided in section S6.

S6. Phase shifter calibration

Accurate realization of the unitary transformations requires calibrating the titanium nitride (TiN) resistive heaters integrated in each MZI. The total phase accumulated in each MZI consists of both an electrically-controlled contribution and a fabrication-induced static offset:

$$\alpha_{\text{total}}(I) = \alpha_{\text{elec}}(I) + \alpha_{\text{static}}, \tag{S13}$$

where α represents either θ or φ and I is the applied current.

We empirically find that the heater voltage follows $V = aI^3 + cI + d$, indicating a temperature-dependent resistance $R(I) = aI^2 + c$ arising from the resistivity increase with heating. The dissipated power $P = I^2 R(I)$ induces a phase shift through:

$$\alpha_{\text{total}}(I) = \beta(aI^4 + cI^2) + \alpha_{\text{static}}, \tag{S14}$$

where β is the thermo-optic efficiency coefficient.

We characterize each MZI through two sequential measurements. First, we perform resistance characterization with current-voltage measurements from 0 to 1.35 mA in 10 steps, extracting coefficients a, c, and d. Second, we route light exclusively through the target MZI and measure transmitted optical power while sweeping the current in 50 steps. Using the resistance model from the first measurement, we calculate the heating power at each current and spaced these measurements uniformly in power. The optical power follows a sinusoidal modulation with heating power:

$$P_{\text{out}} = P_{\text{avg}}[1 \pm \cos(\omega P_{\text{heat}} + \phi_0)], \tag{S15}$$

where $P_{heat} = aI^4 + cI^2$ and the sign $(\pm)$ depends on the measurement configuration, with opposite input-output ports giving the cross configuration (+) and the same ports giving the bar configuration (-). Fitting this response yields $\omega = \beta$ and $\phi_0 = \alpha_{\text{static}}$, enabling the calculation of the required current for any target phase through numerical solution of Eq. (S14).

This fitting procedure applies to both internal and external phase shifters. While internal phases require routing light exclusively through individual MZIs [**?**], external phases require extended interferometric configurations for characterization [**?**].

S7. Measurement protocol and error analysis

For each discretized time step t, the ideal unitary $U(t)$ was decomposed into the required phase shifts. These phases were applied to the thermo-optic phase shifters with a 1-second dwell time to ensure thermal steady state before acquisition. The output signals were collected using a MEMS optical switch synchronized with the power meter. A switching delay of 50 ms was enforced between ports to ensure mechanical stability. The optical power at each port was recorded as the average of 20 hardware samples.

We treated each raw reading as having a $\pm 3\%$ relative uncertainty. To account for variations in fiber-to-chip coupling efficiency, we normalized the measured powers at each time step. The population at site i was calculated as:

$$P_i = \frac{P_{i,\text{raw}}}{\sum_j P_{j,\text{raw}}}, \tag{S16}$$

where $P_{i,\text{raw}}$ denotes the raw measured power at site i and the sum extends over all active lattice sites. Assuming independent channel errors with $\sigma(P_{j,\text{raw}}) = r\, P_{j,\text{raw}}$, the corresponding 1σ uncertainty on the normalized populations was obtained by standard error propagation:

$$\sigma(P_i) = r\, P_i \sqrt{1 + \sum_j P_j^2 - 2P_i}\,, \qquad r = 0.03, \tag{S17}$$

and we report $P_i \pm \sigma(P_i)$ throughout.

S8. Extended simulation of seven-site transport

To extend the main-text results, we simulate the seven-site hexagon over a longer evolution window of $9T$, see fig. S3. This allows us to confirm that the directional transport is not a short-time artifact but persists across multiple cycles. In this regime, the circulating multi-peak/single-peak structure executes more than one full rotation around the perimeter, demonstrating sustained chiral motion.

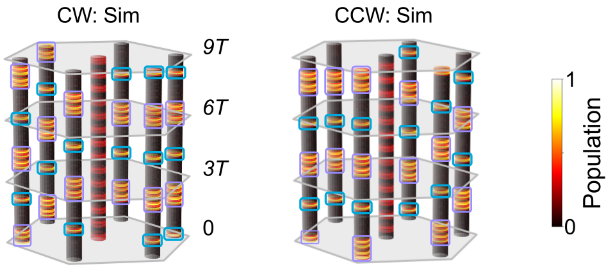

Fig. S3. Extended seven-site dynamics. Simulated evolution under CW (left) and CCW (right) drives at the gap-optimized period $T = 13.6647$, using 15 steps per period. Horizontal planes mark 0, $3T$, $6T$, $9T$. The characteristic multi-peak/single-peak pattern described in the main text persists over long times, advancing chirally around the perimeter and completing on the order of two full rotations. Violet boxes mark the multi-peak packet and cyan boxes mark the single-peak packet; for clarity, arrows used in the main-text are omitted here.